

LETTER TO THE EDITOR

Discovery of the acetyl cation, CH_3CO^+ , in space and in the laboratory [★]

J. Cernicharo¹, C. Cabezas¹, S. Bailleux², L. Margulès², R. Motiyenko², L. Zou², Y. Endo³, C. Bermúdez¹, M. Agúndez¹, N. Marcelino¹, B. Lefloch⁴, B. Tercero^{5,6}, and P. de Vicente⁵

¹ Grupo de Astrofísica Molecular, Instituto de Física Fundamental (IFF-CSIC), C/ Serrano 121, 28006 Madrid, Spain. e-mail: jose.cernicharo@csic.es

² Univ. Lille, CNRS, UMR 8523 - PhLAM - Physique des Lasers Atomes et Molécules, 59000 Lille, France

³ Department of Applied Chemistry, Science Building II, National Chiao Tung University, 1001 Ta-Hsueh Rd., Hsinchu 30010, Taiwan

⁴ CNRS, IPAG, Univ. Grenoble Alpes, F-38000 Grenoble, France

⁵ Observatorio Astronómico Nacional (IGN), C/ Alfonso XII, 3, 28014, Madrid, Spain.

⁶ Centro de Desarrollos Tecnológicos, Observatorio de Yebes (IGN), 19141 Yebes, Guadalajara, Spain.

Received; accepted

ABSTRACT

Using the Yebes 40m and IRAM 30m radiotelescopes, we detected two series of harmonically related lines in space that can be fitted to a symmetric rotor. The lines have been seen towards the cold dense cores TMC-1, L483, L1527, and L1544. High level of theory *ab initio* calculations indicate that the best possible candidate is the acetyl cation, CH_3CO^+ , which is the most stable product resulting from the protonation of ketene. We have produced this species in the laboratory and observed its rotational transitions $J_u = 10$ up to $J_u = 27$. Hence, we report the discovery of CH_3CO^+ in space based on our observations, theoretical calculations, and laboratory experiments. The derived rotational and distortion constants allow us to predict the spectrum of CH_3CO^+ with high accuracy up to 500 GHz. We derive an abundance ratio $N(\text{H}_2\text{CCO})/N(\text{CH}_3\text{CO}^+) \sim 44$. The high abundance of the protonated form of H_2CCO is due to the high proton affinity of the neutral species. The other isomer, H_2CCOH^+ , is found to be $178.9 \text{ kJ mol}^{-1}$ above CH_3CO^+ . The observed intensity ratio between the $K=0$ and $K=1$ lines, ~ 2.2 , strongly suggests that the *A* and *E* symmetry states have suffered interconversion processes due to collisions with H and/or H_2 , or during their formation through the reaction of H_3^+ with H_2CCO .

Key words. Astrochemistry — ISM: molecules — ISM: individual (TMC-1) — line: identification — molecular data

1. Introduction

The cold dark core TMC-1 presents an interesting chemistry. It produces a significant number of the molecules detected in space, in particular long neutral carbon-chain radicals and their anions (see e.g. Cernicharo et al. 2020a; Marcelino et al. 2020a, and references therein) as well as cyanopolynes (see Cernicharo et al. 2020b and Xue et al. 2020, and references therein). The presence in this object of O-bearing carbon chains, such as C_2O (Ohishi et al. 1991), C_3O (Matthews et al. 1984), HC_5O (McGuire et al. 2017), HC_7O (Cordiner et al. 2017), HCCO , and HC_3O^+ (Cernicharo et al. 2020c), is a surprising result that has not yet been fully accounted for by chemical models.

The abundance of polyatomic cations in cold interstellar clouds is relatively low because they react fast with electrons. Interestingly, all polyatomic cations detected in cold clouds are protonated forms of stable and abundant molecules. Chemical models and observations suggest a trend in which the protonated-to-neutral abundance ratio $[\text{MH}^+]/[\text{M}]$ increases with

the proton affinity of M (Agúndez et al. 2015; Cernicharo et al. 2020c,d; Marcelino et al. 2020a).

It has been suggested that some O-bearing cations are sufficiently long-lived to be abundant (Petrie et al. 1993). We have recently reported the discovery of the cation HC_3O^+ in TMC-1 (Cernicharo et al. 2020c). In this letter, we report the detection of two series of lines that are harmonically related towards the cold dark core TMC-1. These lines can be fitted as the $K=0$ and $K=1$ lines of a symmetric rotor. From the astronomical data and the derived rotational constants, together with high-level *ab initio* calculations, we suggest CH_3CO^+ as the best possible carrier. We have performed microwave laboratory experiments that fully support this hypothesis: We detected 79 rotational transitions near the predicted frequencies from the astronomical constants. Hence, we report the discovery in space and in the laboratory of CH_3CO^+ (acetyl cation), which is the most stable isomer resulting from the protonation of ketene (H_2CCO). The presence of CH_3CO^+ can be expected on the basis of the high abundance of H_2CCO in TMC-1 and its large proton affinity ($825.3 \text{ kJ mol}^{-1}$; Traeger et al. 1982). An anomalous abundance ratio of 2.2 is found between the *A* and *E* symmetry species of CH_3CO^+ . We discuss these results in the context of state-of-the-art chemical models and in terms of the interconversion of *E*- CH_3CO^+ into *A*- CH_3CO^+ through the formation process of the molecule or by collisions with H and/or H_2 .

[★] Based on observations carried out with the Yebes 40m telescope (projects 19A003, 20A014, and 20D15) and the Institut de Radioastronomie Millimétrique (IRAM) 30m telescope. The 40m radiotelescope at Yebes Observatory is operated by the Spanish Geographic Institute (IGN, Ministerio de Transportes, Movilidad y Agenda Urbana). IRAM is supported by INSU/CNRS (France), MPG (Germany), and IGN (Spain).

2. Observations

New receivers, built as part of the Nanocosmos project¹ and installed at the Yebes 40m radio telescope, were used for the observations of TMC-1. The Q-band receiver consists of two high electron mobility transistor (HEMT) cold amplifiers that cover the 31.0-50.3 GHz band with horizontal and vertical polarizations. Receiver temperatures vary from 22 K at 32 GHz to 42 K at 50 GHz. The spectrometers are $2 \times 8 \times 2.5$ GHz fast Fourier transform spectrometers (FFTs) with a spectral resolution of 38.1 kHz, providing the whole coverage of the Q-band in both polarizations. The main beam efficiency varies from 0.6 at 32 GHz to 0.43 at 50 GHz (Tercero et al. 2020).

The observations that led to the line survey in the Q-band towards TMC-1 ($\alpha_{J2000} = 4^h41^m41.9^s$ and $\delta_{J2000} = +25^\circ41'27.0''$) were performed in several sessions, between November 2019 and February 2020. The observing procedure was frequency switching with a frequency throw of 10 MHz. The nominal spectral resolution of 38.1 kHz was used for the final spectra. In these runs, two different frequency coverages were observed, 31.08-49.52 GHz and 31.98-50.42 GHz. This permits the user to check that no spurious ghosts are produced in the down-conversion chain, in which the signal coming from the receiver is down-converted to 1-19.5 GHz and then split into eight bands with a coverage of 2.5 GHz, each of which are analysed by the FFTs. Additional data were taken in October 2020 to improve the line survey at some frequencies and to further check the consistency of all observed spectral features. These observations were also performed in frequency switching but with a throw of 8 MHz. The sensitivity varies along the Q-band between 0.5 and 2.5 mK, which is a considerable improvement compared to previous line surveys in the 31-50 GHz frequency range (Kaifu et al. 2004).

The IRAM 30m data come from a line survey performed towards TMC-1 and B1, and the observations have been described by Marcelino et al. (2007) and Cernicharo et al. (2012). The observations of L1527 and L1544 were obtained as part of the IRAM 30m Large Program ASAI and were described by Lefloch et al. (2018). The intensity scale and antenna temperature (T_A^*) for the two telescopes used in this work were calibrated using two absorbers at different temperatures as well as the atmospheric transmission model ATM (Cernicharo 1985; Pardo et al. 2001). Calibration uncertainties were adopted to be 10 %. All data were analysed using the GILDAS package².

3. Results and discussion

The assignment of the observed features in our line surveys was done using the CDMS and JPL catalogues (Müller et al. 2005; Pickett 1998) and the MADEx code (Cernicharo 2012). Most of the weak lines found in our survey of TMC-1 can be assigned to known species and their isotopologues. Nevertheless, many features remain unidentified. Frequencies for the unknown lines were derived by assuming a local standard of rest velocity of 5.83 km s^{-1} , a value that was derived from the observed transitions of HC_5N and its isotopologues in our line survey (Cernicharo et al. 2020a,b). Our new data towards TMC-1 allowed us to detect C_3N^- and C_5N^- (Cernicharo et al. 2020a), as well as new species such as the isocyan isomer of HC_5N , HC_4NC (Cernicharo et al. 2020b), the cation HC_3O^+ (Cernicharo et al. 2020c), the cation HC_3S^+ (Cernicharo et al. 2020d), and the cation HC_5NH^+ (Marcelino et al. 2020a), in addition to several tens of already known molecules and their isotopologues.

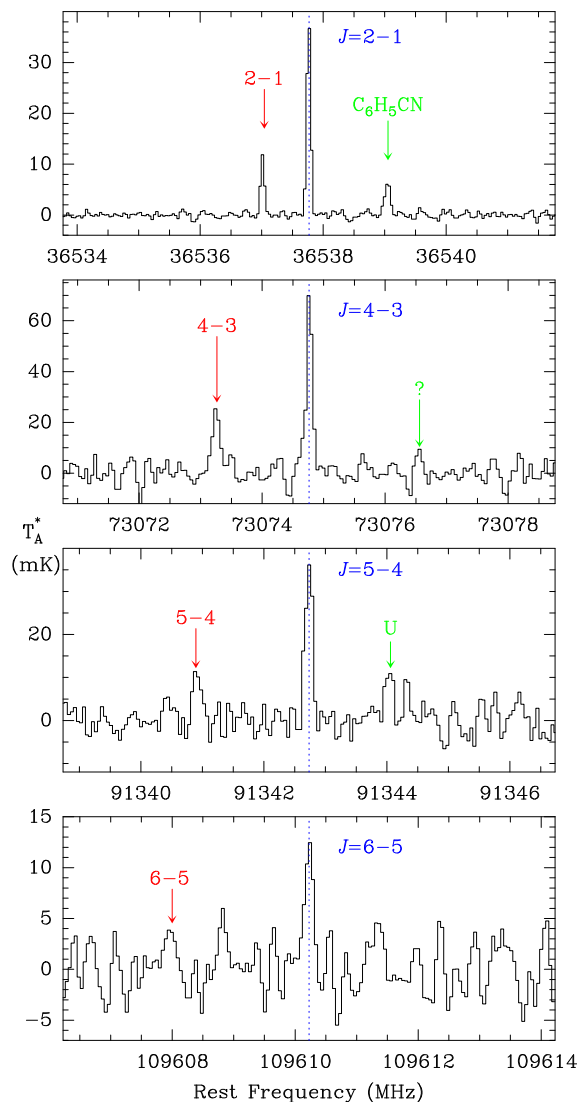


Fig. 1. Observed lines of CH_3CO^+ towards TMC-1. The abscissa corresponds to rest frequencies (in MHz) assuming a local standard of rest velocity of 5.83 km s^{-1} (Cernicharo et al. 2020a,b). Frequencies and intensities for the observed lines are given in Table 1. The ordinate is the antenna temperature (in mK). Spectral resolution is 38.1 kHz below 50 GHz and 48.8 kHz above. The blue labels correspond to the series of lines we assign to the A species of CH_3CO^+ , while the red ones correspond to those of the E species.

Table 1. Observed line parameters for CH_3CO^+ in TMC-1.

J_u	K	ν_{obs}^a (MHz)	$\Delta\nu_{\text{oc}}^b$ (kHz)	T_A^c (mK)	$\Delta\nu^d$ (km s^{-1})	$\int T_A^* dv^e$ (mK km s^{-1})
2	0	36537.765	-3.5	39.0 ± 0.6	0.63 ± 0.01	26.1 ± 0.6
2	1	36537.014	-0.6	11.8 ± 0.6	0.60 ± 0.03	7.5 ± 0.6
4	0	73074.769	2.7	71.0 ± 3.5	0.47 ± 0.03	35.7 ± 2.0
4	1	73073.252	-6.6	25.0 ± 3.5	0.65 ± 0.11	17.2 ± 2.0
5	0	91342.732	-3.5	37.5 ± 3.0	0.46 ± 0.04	18.2 ± 1.0
5	1	91340.865	14.2	11.9 ± 3.0	0.49 ± 0.11	6.3 ± 1.0
6	0	109610.225	2.1	12.8 ± 2.8	0.45 ± 0.09	6.1 ± 1.0
6	1	109607.954	-7.3	6.6 ± 2.8	0.60 ± 0.10	4.2 ± 1.0

Notes. ^(a) Observed frequencies (in MHz) adopting a v_{LSR} of 5.83 km s^{-1} for TMC-1. The uncertainty is 10 kHz for all the lines. ^(b) Observed minus calculated frequencies (in kHz) resulting from a fit to the observed frequencies. The $J=7-6$ $K=0,1$ lines observed in L1527 have been included in the fit (see text). ^(c) Antenna temperature (in mK). ^(d) Linewidth at half intensity (in km s^{-1}). ^(e) Integrated line intensity (in mK km s^{-1}).

¹ <https://nanocosmos.iff.csic.es/>

² <http://www.iram.fr/IRAMFR/GILDAS>

Table 2. Derived spectroscopic parameters (in MHz) for CH_3CO^+ .

Constant	Space ^a	Laboratory ^b	Merged ^c
B	9134.47424(82)	9134.47083(27)	9134.47211(20)
D_J	4.014(12) 10^{-3}	3.99198(25) 10^{-3}	3.99307(21) 10^{-3}
D_{JK}	1.8847(53) 10^{-1}	1.87616(41) 10^{-1}	1.87736(46) 10^{-1}
H_{JK}		8.66(33) 10^{-7}	9.56(37) 10^{-7}
H_{KJ}		6.58(59) 10^{-6}	7.19(74) 10^{-6}
$rms(\text{kHz})^d$	6.9	34.3	33.2
J_{min}/J_{max}	1/7	10/27	1/27
K_{min}/K_{max}	0/1	0/6	0/6
N_{lines}^e	10	79	89
$\nu_{max}(\text{GHz})$	127.87	492.95	492.95

Notes. ^(a) Fit to the lines of CH_3CO^+ observed in TMC-1. In this fit, the $J=7-6$ and $K=0,1$ lines observed in L1527 (with frequencies of 127877.133 ± 0.025 and 127874.494 ± 0.050 MHz, respectively) have been included (see Fig. A.1 and Appendix A). ^(b) Fit to the lines of CH_3CO^+ observed in the laboratory. ^(c) Fit to the lines of CH_3CO^+ observed in space and in the laboratory. ^(d) The standard deviation of the fit (in kHz). ^(e) Number of lines included in the fit.

Within the unidentified features in our surveys in the 3 mm band and the Q-band, we found two series of four lines with a harmonic relation of 2:4:5:6 (see Fig. 1). Taking into account the line density in TMC-1, the possibility that the observed pattern is fortuitous is very small. The observed lines are shown in Fig. 1, and the derived line parameters are given in Table 1. In fact, the $J=5-4$ line at 91342 MHz has intrigued us since 2017 when we detected it in TMC-1, L483, L1527, and L1544. We interpreted the $K=0,1$ lines and the U line at ~ 91344 (see Fig. A.1) as the hyperfine structure of a $J=1-0$ or $J=2-1$ transition of a molecule containing a nucleus with a spin of 1. Using the old receivers of the Yebes 40 m telescope, and assuming that the three lines around 91342 MHz could correspond to $J=2-1$, we searched for lines at 45671 MHz without success. Only when the new receivers covering the whole Q-band were available at the telescope, and we detected the doublet at 36537 MHz (see Fig. 1), did we realized that two of the lines around 91342 MHz correspond to a $J=5-4$ transition in harmonic relation 2:5 with the 36537 MHz doublet. Moreover, the U line at 91344 MHz is produced by another carrier as it is detected in B1, while the other lines are not. Once we relaxed the initial idea that these features were the hyperfine structure of a low- J transition, other features were found in the 3 mm domain ($J=4-3$ and $J=6-5$, as well as $J=7-6$ in L1527).

The two series of lines can be fitted to two linear rotors with rotational constants $B = 9134.4738 \pm 0.0006$ MHz and $B = 9134.2860 \pm 0.0020$ MHz. The distortion constant is exactly the same for both series, $D = 4.00 \pm 0.02$ kHz. The observed spectra is reminiscent of the $K=0$ and $K=1$ components of the rotational transitions of a symmetric rotor. In fact, the eight observed lines in TMC-1 can be fitted with a single rotational constant and two distortion constants if we assume that the carrier is the same for both series and that it has a C_{3v} symmetry (i.e. that it is a symmetric rotor). Using the standard Hamiltonian for this kind of molecular rotor (Gordy & Cook 1984), we derived the rotational and distortion constants provided in Table 2.

From the derived rotational constant, 9134 MHz, the molecule should contain at least three atoms between C, N, and O. We analysed the possible candidates that could have a rotational constant similar to the observed one. Detailed *ab initio* calculations for the possible linear and asymmetric carriers are given in Appendix B. Concerning symmetric rotors, it is amazing to realize that all CH_3X , with $\text{X}=\text{CN}$, NC , and CCH , have rotational constants close to our rotational and distortion con-

Table 3. Scaled theoretical values for the spectroscopic parameters of CH_3CO^+ , CH_2COH^+ , and CH_3NCH^+ together with the experimental values obtained in this work (all in MHz).

Parameter	Exp. ^a	CH_3CO^+	CH_2COH^+	CH_3NCH^+
B	9134.4742(8)	9129.6	9309.5 ^b	9105.5
$D_J \times 10^{-3}$	4.014(13)	3.9	2.8	4.0
$D_{JK} \times 10^{-3}$	188.47(50)	184.6	378.7	171.7

Notes. ^(a) This work. ^(b) $(B+C)/2$

stants. For example, CH_3CN has a rotational constant of 9198.9 MHz (Müller et al. 2009), which is really very close to our result. The other possible candidates, CH_3CNH^+ ($B=8590.5$ MHz; Amano et al. 2006) and CH_3NCH^+ (see, Table B.1), are too heavy. Hence, the best symmetric rotor candidate seems to be a species similar to CH_3CN . The acetyl radical, CH_3CO , has been observed in the laboratory by Hirota et al. (2006), but it is asymmetric and its lines show a very complex hyperfine structure. However, CH_3CO^+ is a symmetric rotor (Mosley et al., 2014) and the lowest energy isomer of $\text{H}_3\text{C}_2\text{O}^+$. Its possible precursor, if formed through protonation, is ketene, which is one of the most abundant O-bearing species in TMC-1 (see Cernicharo et al. 2020c).

3.1. Quantum chemical calculations and assignment to CH_3CO^+

Precise geometries and spectroscopic molecular parameters for the species mentioned above were computed using high-level *ab initio* calculations. The first screening for all plausible candidates (see Appendix B) was done at the CCSD/cc-pVTZ level of theory (Cížek 1969; Dunning 1989). These results are shown in Table B.1. In a second stage, the most promising candidates, namely CH_3CO^+ , CH_2COH^+ , and CH_3NCH^+ , were calculated at the CCSD(T)-F12b/aug-cc-pVQZ levels of theory (Raghavachari et al. 1989; Adler et al. 2007; Knizia et al. 2009). To obtain more precise values for the rotational parameters of these three species, we calibrated our calculations using experimental to theoretical scaling ratios for analogue molecular species. This method has been proved to be suitable to accurately reproduce the molecular geometry of other identified molecules (Cernicharo et al. 2019; Marcelino et al. 2020a; Cernicharo et al. 2020c). In our present case, we used CH_3CN , CH_2CNH , and CH_3NC , which are isoelectronic species of CH_3CO^+ , CH_2COH^+ , and CH_3NCH^+ , respectively, for this purpose. Table B.2 shows the results of these calculations, which are summarized in Table 3. As can be seen, the employed level of theory reproduces the rotational parameters for CH_3CN , CH_2CNH , and CH_3NC very well, with relative discrepancies around 0.08% and 0.04% for B in the cases of CH_3CN and CH_3NC , respectively. After correcting the calculated parameters for CH_3CO^+ , CH_2COH^+ , and CH_3NCH^+ using the derived scaling ratios for CH_3CN , CH_2CNH , and CH_3NC , respectively, we obtained a B constant of 9129.62 MHz for CH_3CO^+ , which shows the best agreement with that derived from the TMC-1 lines. The centrifugal distortion values, obtained in the same manner but at the MP2/aug-cc-pVQZ level of theory for CH_3CO^+ and CH_3NCH^+ , are both compatible with those obtained from the fit of the lines. The agreement between the experimental constants and those calculated for CH_2COH^+ is substantially worse. The calculated dipole moments for CH_3CO^+

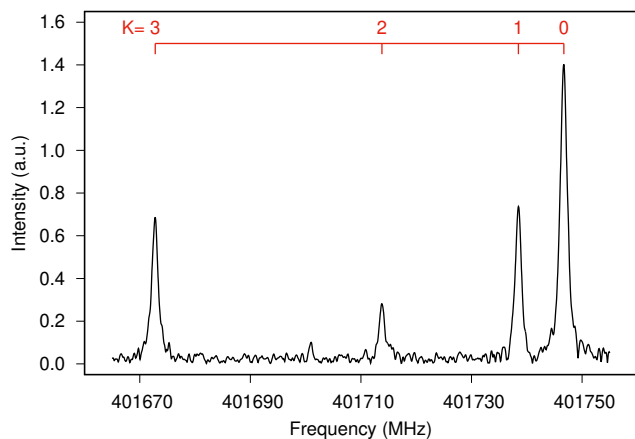


Fig. 2. $J=22\rightarrow 21$, $K=0-3$ transitions obtained by chirped-pulsed excitation. The record corresponds to the average of 67 million spectra acquired in ~ 20 min.

and CH_3NCH^+ are 3.5 D and 2.0 D, respectively, while the μ_a and μ_b values for CH_2COH^+ are 0.8 and 1.7 D, respectively.

In addition to the geometry optimizations, we calculated the energy associated with the plausible formation of CH_3CO^+ , starting from ketene and three proton donors; H_3^+ , H_3O^+ , and HCO^+ . All these calculations were carried out at the CCSD/cc-pVTZ level of theory. We found a total energy change in the protonation of ketene to form CH_3CO^+ of -421.8 , -130.9 , and -244.8 kJ mol^{-1} when ketene reacts with H_3^+ , H_3O^+ , and HCO^+ , respectively. More details can be found in Appendix C.

3.2. Laboratory detection of CH_3CO^+

We conducted an experiment to detect the CH_3CO^+ cation in the laboratory using rotational spectroscopy below 500 GHz. The experimental setup was similar to the one used to detect NS^+ (Cernicharo et al. 2018). The cation was produced in a liquid-nitrogen-cooled Pyrex absorption cell by glow-discharging a mixture of CH_4 , CO (1:1), and Ar. A solenoid coil wound on the cell can generate an axial magnetic field (up to 300 G) to magnetically extend the negative glow, the region known to produce the highest concentrations of cations (compared to the positive column discharge; De Lucia et al. 1983). We also tried acetone and acetaldehyde as precursors (Mosley et al., 2014), but without success.

To optimize the experimental setup, we first observed the $J=2\leftarrow 1$ transition of HCO^+ at 178375.056 MHz, which was produced in the same gas mixture. We then searched for the $J=10\leftarrow 9$, $K=0-2$ series of lines of CH_3CO^+ between 182.658 and 182.675 GHz based on the rotational constants derived from the lines observed in TMC-1. Weak spectra were observed within 500 kHz. The best experimental conditions were found to be $P(\text{CH}_4)=P(\text{CO})=1.5$ mTorr, $P(\text{Ar})=5.5$ mTorr (gas mixture cooled using liquid nitrogen but pressures measured at room temperature), an electric discharge of 3.5 kV/10 mA, and an axial magnetic field of 200 G. These lines disappeared when one of the precursors was suppressed, or when the axial magnetic field was cut off. The latter phenomenon confirmed almost unambiguously that they were due to a cation. Subsequent measurements of higher- J transitions fully support the astrophysical assignment of the observed lines to CH_3CO^+ .

In total, 79 lines were observed in the laboratory with quantum numbers in the ranges $J=10-27$ and $K \leq 6$ (see Table E.1).

Transitions occurring below 330 GHz were measured by standard frequency modulation absorption spectroscopy, resulting in second-derivative lineshapes. These lines ($K \leq 3$) were found unshifted from the first prediction. Those from 400 to 500 GHz were measured by emission spectroscopy (Zou et al. 2020), giving Voigt-profile lineshapes. Compared to the prediction, some deviations were observed up to 1 MHz for $K=6$; these measurements led us to determine the H_{JK} and H_{KJ} centrifugal distortion terms. For maximum sensitivity, these lines were measured using the single frequency excitation method with 5-20 million acquisitions (which took 1 to 5 min.). Additionally, a 120 MHz wide chirped excitation spectrum, measured with 67 million acquisitions, is given in Fig. 2 for illustration and comparison purposes. The uncertainty of the laboratory frequency measurements are estimated to be 50 kHz. Given the mass of the cation, and that the negative glow is a nearly electric field-free region, the reported laboratory frequencies are expected to be unshifted by the Doppler effect. The separate and merged least-squares analysis of all (astronomical and laboratory) measured transitions are provided in Table 2. The measured frequencies and the observed minus calculated values are given in Table E.1. Frequency predictions are given in Table E.2.

3.3. Chemistry of CH_3CO^+

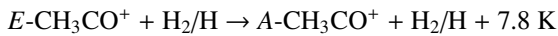
From the observed line intensities of CH_3CO^+ , we derived a rotational temperature of ~ 5 K and a total column density of $(3.2 \pm 0.3) \times 10^{11} \text{ cm}^{-2}$ (see Appendix D). The column densities for the A and E species are $(2.2 \pm 0.2) \times 10^{11} \text{ cm}^{-2}$ and $(9.7 \pm 0.9) \times 10^{10} \text{ cm}^{-2}$, respectively. Adopting the column density for ketene derived by Cernicharo et al. (2020c), we obtained a $\text{H}_2\text{CCO}/\text{CH}_3\text{CO}^+$ ratio of 44. Assuming the H_2 column density derived by Cernicharo & Guélin (1987), the abundance of CH_3CO^+ is 3.2×10^{-11} .

The chemistry of protonated molecules in cold dense clouds has been discussed by Agúndez et al. (2015). Chemical model calculations similar to those that they presented predict that the abundance of protonated ketene is controlled by the typical routes operating for protonated molecules. That is, CH_3CO^+ is mostly formed by proton transfer to H_2CCO from HCO^+ , H_3^+ , and H_3O^+ , while it is destroyed through dissociative recombination with electrons. The radiative association between CH_3^+ and CO is also an important route to CH_3CO^+ . The abundance ratio $\text{H}_2\text{CCO}/\text{CH}_3\text{CO}^+$ predicted by the model is in the range 250-450 and depends on whether the UMIST RATE12 (McElroy et al. 2013) or KIDA kida.uva.2014 (Wakelam et al. 2015) chemical networks are used. As occurs for most protonated molecules observed in cold dense clouds, the abundance of the protonated form with respect to the neutral is underestimated by the chemical model. In this case, there is a factor of 5-10 difference between the model and observations. Incorrect estimates for the rate constants of the dominant reactions of the formation and destruction of CH_3CO^+ may be behind this disagreement. Alternatively, the chemical network may miss some important formation route to CH_3CO^+ , although it is difficult to identify reactions producing this ion from abundant reagents. For example, plausible reactions of CH_n^+ ions with CO , H_2CO , or CH_3OH tend to form products other than CH_3CO^+ (Adams & Smith 1978). In this context, it is worth noting that not all species resulting from the protonation of abundant molecules in TMC-1 are detected. For example, CH_3CNH^+ is not detected in TMC-1 despite the CH_3CN proton affinity of 787.4 ± 5.9 kJ mol^{-1} (Williams et al. 2001). The 3σ upper limit to the column density of CH_3CNH^+ is $2.5 \times 10^{11} \text{ cm}^{-2}$. The column density of

CH_3CN is $(3.2 \pm 0.2) \times 10^{12} \text{ cm}^{-2}$ (see Appendix A); hence, the abundance ratio between the neutral and its protonated form is ≥ 13 . The low dipole moment of CH_3CNH^+ compared to that of CH_3CN (1.01 D versus 3.93 D) limits the chances of detecting this species.

3.4. $A\text{-CH}_3\text{CO}^+ / E\text{-CH}_3\text{CO}^+$ abundance ratio

The column densities derived for the *A* and *E* species of CH_3CO^+ are not identical, as would be expected for a symmetric top. The *A/E* abundance ratio for this molecule is 2.27. However, all symmetric molecules of CH_3X detected in TMC-1 have an abundance ratio between their *A* and *E* species that is close to unity (see Appendix D and Fig. D.2). In a symmetric top, the two symmetry states *A* and *E* are not connected radiatively nor through inelastic collisions with H_2 . Unlike the rest of the CH_3X molecules detected in TMC-1, CH_3CO^+ is a cation, and its reactive collisions with H_2 or H could produce a proton interchange if there is no barrier to the reaction. The lowest energy level of the *E* symmetry state is the $J=1, K=1$, which is 7.8 K above the ground $J=0, K=0$ level of the *A* state. Hence, the reaction of interchange of a proton



is exothermic, although it is unknown if there is a barrier; this is something that has to be established via detailed theoretical calculations. At thermal equilibrium, and for a kinetic temperature of 10 K, the *A/E* abundance ratio could be $e^{0.78} = 2.18$, which is very close to the observed value of 2.27. For neutral molecules with two or more symmetric hydrogens, the proton interchange could be mainly produced through collisions with H^+ , H_3^+ , HCO^+ , and H_3O^+ , which are much less abundant than H_2 and H . In Appendix D, we discuss the *A/E* abundance ratio of all neutral symmetric rotors that have been detected so far in TMC-1, including CH_3NC , which has previously only been observed in two cold dense clouds: L1544 (Jiménez-Serra et al. 2016) and L483 (Agúndez et al. 2019). For all these species, the *A/E* abundance ratio is close to unity.

Alternatively, we could also consider the possibility that the collisional rates of the acetyl cation with H_2 or He are higher for the *A* species than for the *E* species. As the acetyl cation is isoelectronic to CH_3CN , we could use the collisional rates of the latter species (Khalifa et al. 2020) to estimate possible differences in the excitation temperature of the $K=0$ and $K=1$ lines. We explored a density range of $(4 - 10) \times 10^4 \text{ cm}^{-3}$ and a kinetic temperature range of 5-10 K. No significant differences were found in the predicted brightness temperature between these lines. Of course, if the effect is due to inelastic collisions, then methyl cyanide (CH_3CN) would also show a similar behaviour. Nevertheless, although both species are isoelectronic, the fact that CH_3CO^+ is positively charged could result in very different collisional rates with H_2 compared to CH_3CN .

We could also consider that the *A/E* abundance ratio is affected by the formation process of the molecule. As shown in Sect. 3.1, the reaction of ketene with H_3^+ is the most favourable for protonation from the thermodynamical point of view. Both species, ketene and H_3^+ , could also have their ortho/para ratio affected by the low temperature of dense dark clouds, which will introduce a non-trivial spin statistic into the formation process of CH_3CO^+ . Additional calculations are needed to evaluate the role of collisional excitation and of spin interchange in order to understand the anomalous behaviour exhibited by the *A* and *E* symmetry species of CH_3CO^+ .

Acknowledgements. The Spanish authors thank Ministerio de Ciencia e Innovación for funding support through project AYA2016-75066-C2-1-P, PID2019-106235GB-I00 and PID2019-107115GB-C21 / AEI / 10.13039/501100011033. We also thank ERC for funding through grant ERC-2013-Syg-610256-NANOCOSMOS. MA and CB thanks Ministerio de Ciencia e Innovación for grants RyC-2014-16277 and FJCI-2016-27983, respectively. Y. Endo thanks Ministry of Science and Technology of Taiwan through grant MOST108-2113-M-009-25. We would like to thank Evelyn Roueff and Octavio Roncero for useful comments and suggestions.

References

- Adams, N. G. & Smith, D. 1978, *Chem. Phys. Lett.*, 54, 530
 Adler, T. B., Knizia, G., Werner, H.-J. 2007, *J. Chem. Phys.* 127, 221106
 Agúndez, M., Cernicharo, J., de Vicente, P., et al. 2015, *A&A*, 579, L10
 Agúndez, M., Marcelino, N., Cernicharo, J., et al. 2019, *A&A*, 625, A147
 Amano, T., Hashimoto, K., Hirao, T. 2006, *J. Mol. Struct.*, 795, 190
 Cernicharo, J. 1985, Internal IRAM report (Granada: IRAM)
 Cernicharo, J., & Guélin, M. 1987, *A&A*, 176, 299
 Cernicharo, J., 2012, in *ECLA 2011: Proc. of the European Conference on Laboratory Astrophysics*, EAS Publications Series, 2012, Ed.: C. Stehl, C. Joblin, & L. d'Hendecourt (Cambridge: Cambridge Univ. Press), 251; https://nanocosmos.iff.csic.es/?page_id=1619
 Cernicharo, J., Marcelino, N., Rouef, E., et al. 2012, *ApJ*, 759, L43
 Cernicharo, J., Lefloch, B., Agúndez, M., et al. 2018, *ApJ*, 854, L22
 Cernicharo, J., Cabezas, C., Pardo, J. R., et al. 2019, *A&A*, 630, L2
 Cernicharo, J., Marcelino, N., Pardo, J. R., et al. 2020a, *A&A*, 641, L9
 Cernicharo, J., Marcelino, N., Agúndez, M., et al. 2020b, *A&A*, 642, L8
 Cernicharo, J., Marcelino, N., Agúndez, M., et al. 2020c, *A&A*, 642, L17
 Cernicharo, J., Cabezas, C., Endo, Y., et al. 2020d, *A&A*, submitted
 Cízek, J., in "Advances in Chemical Physics" (P. C. Hariharan, Ed.), Vol. 14, 35, Wiley Interscience, New York, 1969
 Cordner, M. A., Chamley, S. B., Kisiel, Z., et al. 2017, *ApJ*, 850, 187
 De Lucia, F. C., Herbst, E., Plummer, G. M., & Blake, G. A. 1983, *J. Chem. Phys.*, 78, 2312
 Dunning, T. H. 1989, *J. Chem. Phys.* 90, 1007
 Fossé, D., Cernicharo, J., Gerin, M., Cox, P., 2001, *ApJ*, 552, 168
 Gordy, W., & Cook, R. L., 1984, *Microwave Molecular Spectra*, Chapter V, Wiley, New York
 Hirota, E., Mizoguchi, A., Ohshima, Y., et al. 2006, *Mol. Phys.*, 105, 455
 Jiménez-Serra, I., Vasyunin, A. I., Caselli, P., et al. 2016, *ApJ*, 830, L6
 Kaifu, N., Ohishi, M., Kawaguchi, K., et al. 2004, *PASJ*, 56, 69
 Khalifa, M. B., Quintas-Sánchez, E., Dawes, R., et al. 2020, *PCCP*, 22, 17494
 Knizia, G., Adler, T. B., & Werner, H.-J. 2009, *J. Chem. Phys.* 130, 054104
 Latanzi, V., Thorwirth, S., Gottlieb, C., & McCarthy, M. C. 2012, *J. Phys. Chem. Lett.*, 3, 3420
 Lefloch, B., Bachiller, R., Ceccarelli, C., et al. 2018, *MNRAS*, 477, 4792
 Marcelino, N., Cernicharo, J., Agúndez, M., et al. 2007, *ApJ*, 665, L127
 Marcelino, N., Cernicharo, J., Tercero, B., et al. 2009, *ApJ*, 690, L27
 Marcelino, N., Brünken, S., Cernicharo, J., et al. 2010, *A&A*, 516, A105
 Marcelino, N., Agúndez, M., Tercero, B., et al. 2020a, *A&A*, 643, L6
 Marcelino, N., Tercero, B., Agúndez, M., & Cernicharo, J. 2020b, *A&A*, submitted
 McElroy, D., Walsh, C., Markwick, A. J., et al. 2013, *A&A*, 550, A36
 McGuire, B. A., Burkhardt, M., Shingledecker, C. N., et al. 2017, *ApJ*, 843, L28
 Matthews, H. E., Irvine, E., Friberg, F. M., et al. 1984, *Nature*, 310, 125
 Mosley, J. D., Young, J. W., & Duncan, M. A. 2014, *J. Chem. Phys.*, 141, 024306
 Müller, H. S. P., Schlöder, F., Stutzki, J., & Winnewisser, G. 2005, *J. Mol. Struct.*, 742, 215
 Müller, H. S. P., Drouin, B. J., & Pearson, J. C. 2009, *A&A*, 506, 1487
 Müller, H. S. P., Maeda, A., Thorwirth, S., et al. 2019, *A&A*, 621, A143
 Neill, J. L., Muckle, M. T., Zaleski, D. P., et al. 2012, *ApJ*, 755, 153
 Ohishi, M., Suzuki, H., Ishikawa, S.-I., et al., 1991, *ApJ*, 380, L39
 Rodler, M., Brown, R. D., Godfrey, P. D., & Tack, L. M. 1984, *Chem. Phys. Lett.*, 110, 447
 Pardo, J. R., Cernicharo, J., & Serabyn, E. 2001, *IEEE Trans. Antennas and Propagation*, 49, 12
 Petrie, S., Bettens, R. P. A., Freeman, C. G., & McEwan, M. J. 1993, *MNRAS*, 264, 862
 Pickett, H. M., & Boyd, T. L. 1979, *J. Mol. Spectrosc.*, 75, 53
 Pickett, H. M., Poynter, R. L., Cohen, E. A., et al. 1998, *J. Quant. Spectrosc. Radiat. Transfer*, 60, 883
 Pliva, J., Le, L. D., Johns, J. W. C., et al. 1995, *J. Mol. Spectrosc.*, 173, 423
 Raghavachari, K., Trucks, G. W., Pople, J. A., & Head-Gordon, M. 1989, *Chem. Phys. Lett.*, 157, 479
 Sakai, N., Sakai, T., Hirota, T., & Yamamoto, S. 2009, *ApJ*, 702, 1025
 Tercero, B., Pardo, J. R., Cernicharo, J., & Goicoechea, J. 2010, *A&A*, 517, A96
 Tercero, B., Vincent, L., Cernicharo, J., et al. 2011, *A&A*, 528, A26
 Tercero, F., López-Pérez, J. A., Gallego, et al., 2020, *A&A*, 645, A37
 Traeger, J. C., McLoughlin, R. G., & Nicholson, A. J. C. 1982, *J. Am. Chem. Soc.* 104, 5318
 Vastel, C., Yamamoto, S., Lefloch, B., & Bachiller, R. 2015, *A&A*, 582, L3
 Wakelam, V., Loison, J.-C., Herbst, E., et al. 2015, *ApJS*, 217, 20
 Williams, T. I., Denault, J. W., & Cooks, R. G. 2001, *Int. J. Mass Spectrom.*, 210, 133
 Xue, C., Willis, E. R., Loomis, R. A., et al. 2020, *ApJ*, 900, L9
 Zou, L., Motiyenko, R. A., Margulès, & L., Alekseev, A. 2020, *Review of Scientific Instruments*, 91, 063104

Appendix A: CH_3CO^+ in other sources

The acetyl cation, CH_3CO^+ , has also been detected towards L483, L1544, and L1527 (see Fig. A.1). However, it is not observed towards Sgr B2 (PRIMOS³ line survey; Neill et al. 2012), towards Orion-KL (Tercero et al. 2010, 2011), or in our line survey of B1 (Marcelino et al. 2007, 2009, 2010; Cernicharo 2012). In the PRIMOS data on SgrB2, a very tentative detection of the $J=1-0$ $K=0$ line could be claimed at a velocity of 80 km s^{-1} . However, only an upper limit can be obtained for the $J=2-1$ transition as this line is heavily blended with a strong line of acetone. It seems, hence, that CH_3CO^+ is typical of cold interstellar clouds.

Appendix B: Potential carriers of the series of lines

All known diatomic species in cold dark clouds have overly large rotational constants compared with those derived from the lines in TMC-1. For example, a molecule containing one S (CS, NS, SO) will have a rotational constant that is too high by more than 12 GHz. Adding one or two H atoms to these combinations of sulphur produces radicals (with overly high rotational constants, such as HCS) or asymmetric rotors such as H_2CS , which is too heavy (Müller et al. 2019). A molecule with two S atoms is, of course, too heavy (for example, $B(\text{S}_2)=8831 \text{ MHz}$; Pickett 1979), and we do not expect to have Si- or P-bearing polyatomic species in this cloud. The first step in finding candidates is to exclude the possibility of having a slightly asymmetric species. In that case, we could expect to have lines corresponding to $K=\pm 1$ at roughly $\pm(B-C)$ from the $K=0$ lines. We searched in the Q-band survey ($J=2-1$) for such a pattern. No lines up to one-fourth of the intensity of the $K=0$ line are observed. Moreover, taking into account that there is no evidence for a radical as a possible carrier, the species resulting from the addition of one hydrogen to the closed-shell asymmetric species HNC, HCOOH, and H_2CCC have to be excluded. However, their protonated species are also, at least in principle, closed-shell species. Hence, possible candidates are H_2CCCH^+ , $\text{CH}_3\text{CCH}_2^+$, HCNOH^+ , HNCOH^+ , HCOOH_2^+ , and CH_3OO^+ , all of which, with the exception of the last one, are protonated forms of known neutral and abundant species in TMC-1. Nevertheless, the resulting molecular structures will be highly asymmetric for most of them, or they are too light or too heavy, as are the cases for H_2CCCH^+ and $\text{CH}_3\text{CCH}_2^+$, respectively. HNCOH^+ is a linear species characterized in the laboratory with a rotational constant of 9955 MHz (Latanzi et al. 2012) and is not detected in our data. Other exotic species, such as NH_2CHOH^+ , $\text{CH}_2\text{ONH}_2^+$, and CH_3NOH^+ , which could result from the protonation of interesting molecules (NH_2CHO for example), are discarded for their molecular asymmetry and because the neutral species have not been observed in TMC-1. Ab initio calculations have been performed for the most promising candidates (see Table B.1), and their isomers and the results are discussed in Sect. 3.1.

Appendix C: Additional quantum chemical calculations for CH_3CO^+

The potential energy surface (PES) for the protonation of ketene has been explored at the CCSD/cc-pVTZ level of theory. In the

³ Access to the entire PRIMOS data set, specifics on the observing strategy, and overall frequency coverage information is available at <http://www.cv.nrao.edu/~aremijan/PRIMOS/>

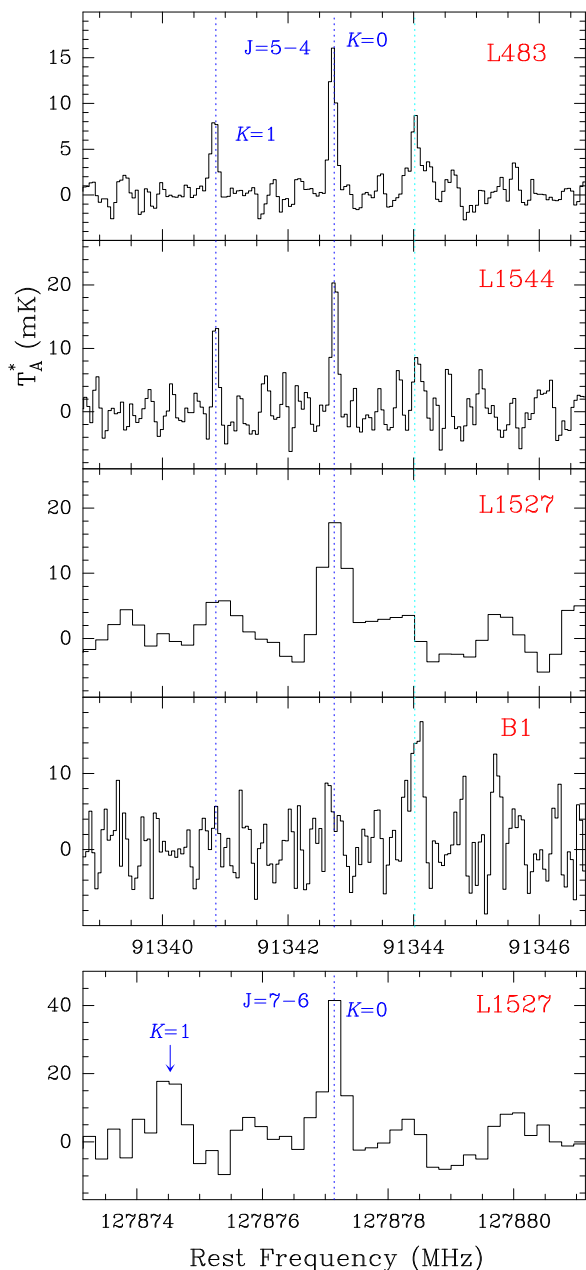
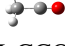
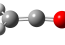
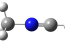
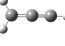
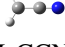





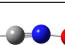
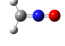

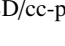


Fig. A.1. Observations of the $J=5-4$ transition of CH_3CO^+ towards L483, L1544, L1527, and B1 (top panels); the bottom panel shows the $J=7-6$ line towards L1527. The abscissa corresponds to the rest frequency (in MHz) and the ordinate is the antenna temperature (in mK). The spectral resolution is 48.8 kHz for all sources except L1527, for which it is 198 kHz. The vertical dashed blue lines indicate the position of the $K=0$ and $K=1$ lines (detected in all sources except B1), and the cyan line corresponds to the U feature at 91344 MHz (detected in all sources except L1527). The rest velocities of L1527 and L1544 were taken as $v_{\text{LSR}} = 5.9 \text{ km/s}$ and 7.2 km/s , respectively, based on Sakai et al. (2009) and Vastel et al. (2015), respectively.

calculations, we considered three possible proton donors: H_3^+ , H_3O^+ , and HCO^+ , as well as the formation of the two isomers of protonated ketene, CH_3CO^+ and CH_2COH^+ . Figure C.1 depicts the PES along the reaction coordinate for the protonation of ketene and the relative energies for all the stationary points when ketene reacts with H_3^+ , H_3O^+ , or HCO^+ . For each reaction, the two reactants, ketene and the proton donor, that separated from each other were assumed to be the energy zero. The protonation

Table B.1. Rotational constants and electric dipole moments of potential candidates.

Species ^(a)	$\Delta E/\text{kJ/mol}^{(b)}$	A, B, C/MHz	$D_J, D_{JK}/\text{kHz}$	$\mu_a, \mu_b, \mu_c/\text{D}$
 H_3CCO^+	0.0	154355.3 9107.2 9107.2	3.9 178.7	2.5 0.0 0.0
 H_2COH^+	178.0	201325.3 9411.2 9222.3	2.7 341.6	1.6 0.1 0.0
 H_3CNCH^+	0.0	155571.2 9090.7 9090.7	3.8 160.6	1.9 0.0 0.0
 H_2CCCH^+	0.0	285625.5 9673.5 9356.6	2.6 457.3	0.5 0.0 0.0
 H_2CCN^+	0.0	280905.8 10338.2 9971.2	3.5 492.0	5.0 0.0 0.0
 H_2CNC^+	5.9	277331.4 11582.1 11117.8	4.00 685.4	3.7 0.0 0.0
 HNCCH^+	102.5	595150.6 10359.3 10182.1	2.7 1285.8	1.5 1.9 0.0
 H_2NCC^+	176.4	328396.0 10180.7 9874.5	3.6 593.3	4.6 0.0 0.0
 HCNCH^+	196.2	11120.9	2.9	0.0
 H_2NCO^+	0.0	324210.9 10295.5 9978.6	2.9 380.4	3.8 0.0 0.0
 HNCOH^+	70.4	723374.4 10034.0 9896.7	2.8 1255.3	1.3 1.7 0.0
 HCNOH^+	285.4	625942.1 10400.0 10230.0	3.8 1859.1	2.4 1.6 0.0
 H_2CNO^+	333.8	268002.3 11140.1 10695.5	3.6 461.1	2.9 0.0 0.0
 H_2CON^+	613.2	259994.7 11321.2 10848.8	4.6 484.7	2.3 0.0 0.0

Notes. ^(a) Calculations at the CCSD/cc-pVTZ level of theory. ^(b) The energy taken as reference is the lowest energy species within the same isomer family.

of ketene in the CH_2 in the three cases is exothermic, and it proceeds without any transition state (TS) to form CH_3CO^+ . This formation is more favourable in the case of H_3^+ . On the other hand, the formation of CH_2COH^+ is exothermic in the cases of H_3^+ and HCO^+ , but endothermic in the case of H_3O^+ . The less stable isomer, CH_2COH^+ , can interconvert through a hydrogen migration to CH_3CO^+ , which has a TS barrier height of 210.1 kJ/mol. As shown in Figure C.1, the TS for this interconversion lies over the energy of the reactants in the protonation of ketene with H_3O^+ and HCO^+ . In contrast, this TS lies below the energy of the reactants when ketene reacts with H_3^+ .

Appendix D: CH_3X species in TMC-1

As noted above, the intensity of the $J=2-1$ $K=1$ line in TMC-1 is well below the expected value if the rotational temperature for the A and E species is the same. In order to check this point, we show in Fig. D.1 the rotational diagrams for the A and E species of CH_3CO^+ using the observed line parameters given in Table 1. The observed intensities have been corrected for beam dilution and the beam efficiencies of the Yebes 40m and IRAM 30m telescopes. We assumed a uniform source of radius $40''$ (Fossé et al. 2001). The derived rotational temperatures, $T_{\text{rot}}(\text{A})=4.4\pm0.4$ K and $T_{\text{rot}}(\text{E})=5.0\pm0.5$ K, are consistent with a common excitation through collisions with H_2 . The de-

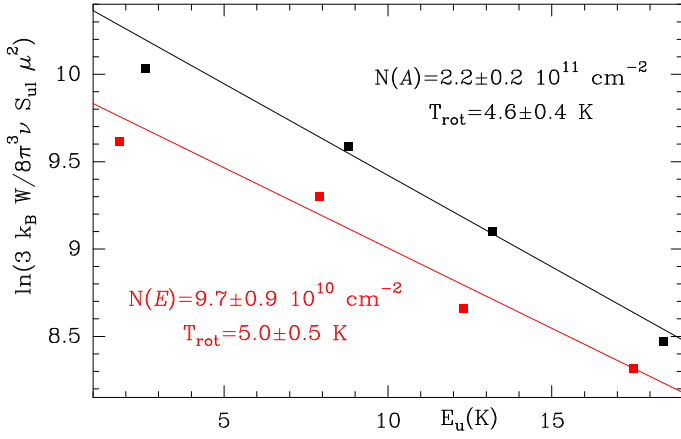


Fig. D.1. Rotational diagrams for the A (black line) and E (red line) symmetry species of CH_3CO^+ in TMC-1.

perature of 10 K and a source radius of $40''$ (Fossé et al. 2001), and we produced a synthetic spectrum that is compared to the observations. We found that the A/E abundance ratio is ≈ 1 for all species but CH_3CO^+ . Adopting a lower rotational temperature has little effect on the derived A/E abundance ratio for these symmetric rotors.

Appendix E: Observed and calculated frequencies of CH_3CO^+

The frequencies observed in space and in the laboratory were merged to obtain the recommended rotational and distortion constants. A total of 89 rotational transitions, ten in space (see Table 1) and 79 in the laboratory (see Table E.1), were fitted to the standard Hamiltonian of a symmetric rotor (Gordy & Cook 1984). For the lines observed in TMC-1 and other dark clouds, only B , D_J , and D_{JK} can be obtained as only rotational transitions with $K=0$ and 1 have been observed. The results are given in Table 2. For the 79 lines observed in the laboratory, the constants H_{JK} and H_{KJ} were included in the fit, and the results are given in Table 2. Finally, the merged fit to the astronomical and laboratory lines produces the recommended set of rotational constants given in the last column of Table 2. The observed and calculated frequencies, together with the observed minus calculated values for the merged fit, are given in Table E.1.

We used the rotational and distortion constants that resulted from the merged fit to the astronomical and laboratory lines (see Table 2) to produce frequency predictions, frequency uncertainties, line strengths, upper energy levels, and Einstein coefficients for all transitions involving levels with energies below 2000 K. They are given in Table E.2. The whole table is electronically available at the CDS. It should be noted that this table contains the transitions for the A and E species, and that the E lowest energy level, $J_K=1_1$, is 7.8 K above the 0_0 level of the A species.

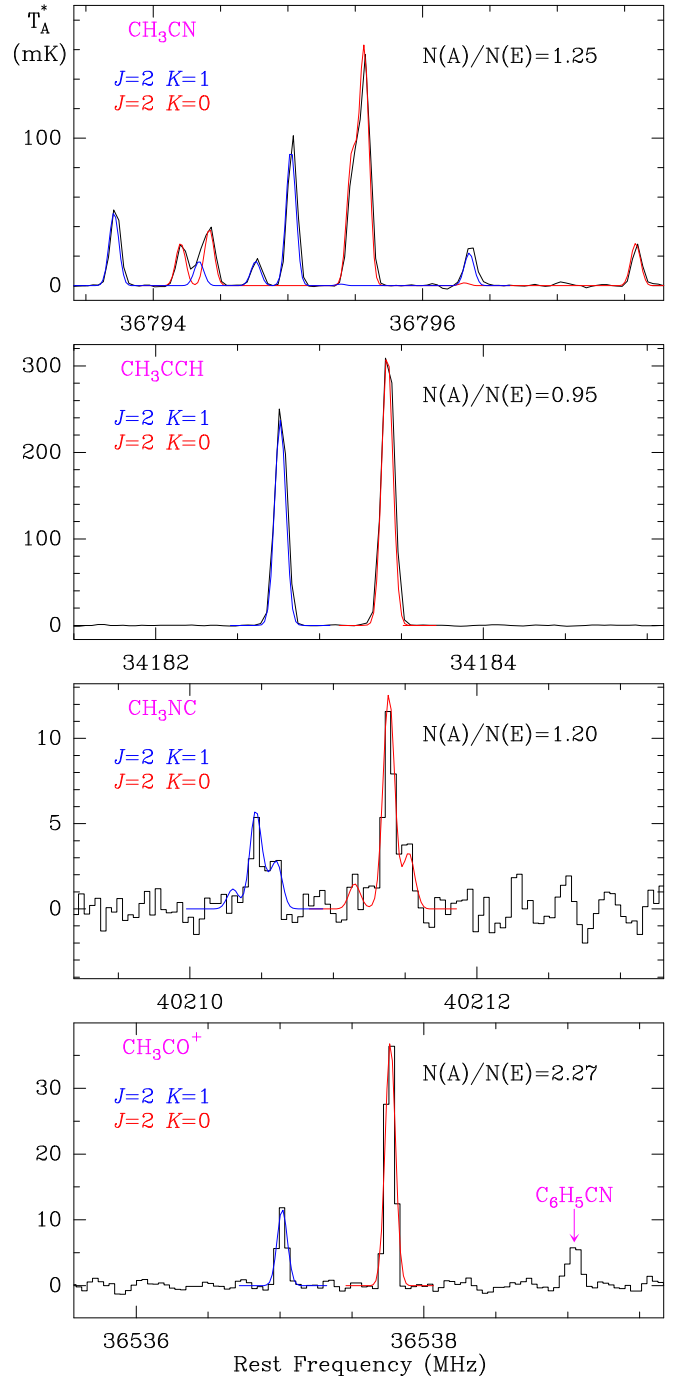


Fig. D.2. Observed lines in the transition $J=2-1$ $K=0,1$ of different symmetric rotors in TMC-1. The colour lines represent the expected line profiles for the A species (red) and E species (blue). The abundance ratio between them in the model is indicated in each panel.

Table E.1. Observed and calculated frequencies (in MHz) for CH₃CO⁺.

J_u	K	Freq. Obser.	(Unc)	Freq. Calc.	(Unc)	Obs-Calc
2	0	36537.765	0.010	36537.761	0.001	0.004
2	1	36537.014	0.010	36537.010	0.001	0.004
4	0	73074.769	0.010	73074.755	0.002	0.014
4	1	73073.252	0.010	73073.253	0.002	-0.001
5	0	91342.732	0.010	91342.725	0.003	0.007
5	1	91340.865	0.010	91340.848	0.003	0.017
6	0	109610.225	0.010	109610.215	0.003	0.010
6	1	109607.954	0.010	109607.963	0.003	-0.009
7	0	127877.133	0.025	127877.131	0.004	0.002
7	1	127874.494	0.050	127874.504	0.004	-0.010
10	3	182639.714	0.050	182639.724	0.011	-0.010
10	2	182658.451	0.050	182658.469	0.006	-0.018
10	1	182669.687	0.050	182669.719	0.005	-0.032
10	0	182673.442	0.050	182673.470	0.005	-0.028
11	3	200900.043	0.050	200900.014	0.012	0.029
11	2	200920.617	0.050	200920.630	0.007	-0.013
11	1	200933.010	0.050	200933.002	0.006	0.008
11	0	200937.148	0.050	200937.127	0.006	0.021
12	3	219159.236	0.050	219159.253	0.013	-0.017
12	2	219181.747	0.050	219181.737	0.008	0.010
12	1	219195.209	0.050	219195.232	0.006	-0.023
12	0	219199.712	0.050	219199.731	0.006	-0.019
13	3	237417.332	0.050	237417.345	0.014	-0.013
13	2	237441.706	0.050	237441.696	0.008	0.010
13	1	237456.320	0.050	237456.311	0.007	0.009
13	0	237461.178	0.050	237461.184	0.007	-0.006
14	3	255674.171	0.050	255674.193	0.015	-0.022
14	2	255700.388	0.050	255700.410	0.009	-0.022
14	1	255716.107	0.050	255716.145	0.007	-0.038
14	0	255721.370	0.050	255721.391	0.007	-0.021
16	3	292183.778	0.050	292183.777	0.017	0.001
16	2	292213.646	0.050	292213.722	0.010	-0.075
16	1	292231.636	0.050	292231.694	0.008	-0.058
16	0	292237.659	0.050	292237.685	0.008	-0.026
17	3	310436.291	0.050	310436.322	0.019	-0.031
17	2	310468.201	0.100	310468.127	0.011	0.074
17	1	310487.210	0.050	310487.216	0.009	-0.006
17	0	310493.523	0.050	310493.580	0.009	-0.057
18	3	328687.226	0.050	328687.241	0.020	-0.015
18	2	328720.866	0.050	328720.905	0.012	-0.039
18	1	328741.056	0.050	328741.110	0.010	-0.054
18	0	328747.827	0.050	328747.846	0.010	-0.019
21	6	383217.758	0.050	383217.721	0.096	0.037
21	5	383303.931	0.050	383303.862	0.064	0.069
21	4	383374.395	0.050	383374.396	0.041	-0.001
21	3	383429.306	0.050	383429.289	0.025	0.017
21	2	383468.517	0.050	383468.517	0.015	0.000
21	1	383492.044	0.050	383492.060	0.012	-0.016
21	0	383499.892	0.050	383499.910	0.012	-0.018
22	6	401451.192	0.050	401451.205	0.103	-0.013
22	5	401541.411	0.050	401541.408	0.069	0.003
22	4	401615.264	0.050	401615.268	0.044	-0.004
22	3	401672.742	0.050	401672.750	0.027	-0.008
22	2	401713.849	0.050	401713.827	0.017	0.022
22	1	401738.482	0.050	401738.481	0.014	0.001
22	0	401746.707	0.050	401746.700	0.014	0.007
23	6	419682.601	0.050	419682.598	0.111	0.003
23	5	419776.829	0.050	419776.858	0.074	-0.029
23	4	419854.065	0.050	419854.039	0.048	0.026
23	3	419914.100	0.050	419914.106	0.029	-0.006

Table E.1. continued.

J_u	K	Freq. Obser.	(Unc)	Freq. Calc.	(Unc)	Obs-Calc
23	2	419957.037	0.050	419957.031	0.018	0.006
23	1	419982.794	0.050	419982.794	0.015	0.000
23	0	419991.387	0.050	419991.383	0.015	0.004
24	6	437911.779	0.050	437911.807	0.119	-0.026
24	5	438010.092	0.050	438010.117	0.080	-0.025
24	4	438090.613	0.050	438090.615	0.052	-0.002
24	3	438153.261	0.050	438153.263	0.032	-0.002
24	2	438198.039	0.050	438198.033	0.020	0.006
24	1	438224.913	0.050	438224.903	0.016	0.010
24	0	438233.877	0.050	438233.861	0.016	0.016
25	6	456138.764	0.150	456138.735	0.129	0.029
25	5	456240.963	0.150	456241.090	0.087	-0.127
25	4	456324.889	0.050	456324.900	0.056	-0.011
25	3	456390.167	0.050	456390.126	0.034	0.041
25	2	456436.758	0.050	456436.737	0.022	0.021
25	1	456464.703	0.050	456464.712	0.018	-0.009
25	0	456474.048	0.050	456474.039	0.018	0.009
26	5	474469.660	0.050	474469.681	0.094	-0.021
26	4	474556.835	0.050	474556.798	0.061	0.037
26	3	474624.604	0.050	474624.597	0.037	0.007
26	2	474673.034	0.050	474673.048	0.024	-0.014
26	1	474702.158	0.050	474702.127	0.020	0.031
26	0	474711.811	0.050	474711.821	0.020	-0.010
27	5	492695.931	0.150	492695.796	0.102	0.135
27	4	492786.129	0.150	492786.214	0.066	-0.085
27	3	492856.584	0.050	492856.582	0.041	0.002
27	2	492906.862	0.050	492906.869	0.026	-0.007
27	1	492937.060	0.050	492937.050	0.022	0.010
27	0	492947.117	0.050	492947.112	0.022	0.005

Table E.2. Frequency predictions for CH₃CO⁺ *.

J_u^a	K_u^a	J_l^a	K_l^a	$\nu(\text{MHz})^b$	Unc(MHz) ^c	$E_{up}(\text{K})^d$	$A_{ij}(\text{s}^{-1})^e$	S_{ij}^f	g_u^g
1	0	0	0	18268.92826	0.00039	0.9	2.898×10^{-07}	1.0000	3
2	1	1	1	36537.00979	0.00072	9.5	2.086×10^{-06}	1.5000	5
2	0	1	0	36537.76068	0.00079	2.6	2.782×10^{-06}	2.0000	5
3	2	2	2	54801.89688	0.00115	32.8	5.587×10^{-06}	1.6667	7
3	1	2	1	54805.27517	0.00107	12.1	8.941×10^{-06}	2.6667	7
3	0	2	0	54806.40143	0.00117	5.3	1.006×10^{-05}	3.0000	7
4	3	3	3	73061.24457	0.00265	70.7	1.081×10^{-05}	3.5000	18
4	2	3	2	73068.74904	0.00151	36.3	1.854×10^{-05}	3.0000	9
4	1	3	1	73073.25310	0.00141	15.7	2.318×10^{-05}	3.7500	9
4	0	3	0	73074.75469	0.00154	8.8	2.473×10^{-05}	4.0000	9
5	4	4	4	91312.71293	0.00563	123.3	1.776×10^{-05}	1.8000	11
5	3	4	3	91325.83851	0.00326	75.1	3.159×10^{-05}	6.4000	22
5	2	4	2	91335.21824	0.00186	40.7	4.148×10^{-05}	4.2000	11
5	1	4	1	91340.84780	0.00173	20.0	4.741×10^{-05}	4.8000	11
5	0	4	0	91342.72461	0.00189	13.2	4.939×10^{-05}	5.0000	11
6	5	5	5	109553.96919	0.01021	190.5	2.644×10^{-05}	1.8333	13
6	4	5	4	109574.20539	0.00662	128.6	4.810×10^{-05}	3.3333	13
6	3	5	3	109589.95432	0.00384	80.4	6.496×10^{-05}	9.0000	26
6	2	5	2	109601.20873	0.00219	46.0	7.701×10^{-05}	5.3333	13
6	1	5	1	109607.96344	0.00203	25.3	8.425×10^{-05}	5.8333	13
6	0	5	0	109610.21536	0.00223	18.4	8.666×10^{-05}	6.0000	13
7	6	6	6	127782.68995	0.01698	272.3	3.683×10^{-05}	3.7143	30
7	5	6	5	127811.51930	0.01162	196.6	6.805×10^{-05}	3.4286	15
7	4	6	4	127835.12506	0.00755	134.7	9.361×10^{-05}	4.7143	15
7	3	6	3	127853.49637	0.00439	86.5	1.135×10^{-04}	11.4286	30
7	2	6	2	127866.62477	0.00249	52.1	1.278×10^{-04}	6.4286	15
7	1	6	1	127874.50422	0.00232	31.4	1.363×10^{-04}	6.8571	15
7	0	6	0	127877.13111	0.00254	24.5	1.391×10^{-04}	7.0000	15

Notes.

(*) The entire table is electronically available at the CDS via anonymous ftp to cdsarc.u-strasbg.fr (130.79.128.5) or via <http://cdsweb.u-strasbg.fr/cgi-bin/qcat?J/A+A>

(a) Upper and lower J_K quantum numbers.

(b) Predicted frequency (in MHz).

(c) Uncertainty in the predicted frequency (in MHz).

(d) Energy (in K) of the upper energy level of the transition.

(e) Einstein coefficient of the transition (in s⁻¹).

(f) Line strength.

(g) Degeneracy of the upper level. It is $2J+1$ for all levels except for those with $K=3 \times n$ ($n=1,2,\dots$), for which g_u is $2 \times (2J+1)$.